CHAPTER 4

DESIGN, SIMULATION AND EFFICIENCY ENHANCEMENT OF PERIODIC DIELECTRIC LOADED FUNDAMENTAL HARMONIC GYRO-TWT *

Part of this work has been published as:

Akash and M. Thottappan, "Design and Efficiency Enhancement Studies of Periodically Dielectric Loaded W-Band Gyro-TWT Amplifier," *IEEE Trans. on Electron Devices*, vol. 67, no. 7, pp. 2925-2932, July 2020 (doi:10.1109/TED.2020.2996191).

Akash and M. Thottappan, "Design, Beam-Wave Interaction, and Efficiency Enhancement Studies of Millimeter Wave Gyro-TWT with a Three-Stage Depressed Collector," *IEEE Trans. on Plasma Scie.*, vol. 48, no. 6, pp. 1930-1935, June 2020 (10.1109/TPS.2020.2978792).

4.1. Introduction

A wave particle interaction system with periodic dielectric loading over the linear section (more practical case of dielectric loading) has been employed to avoid the dielectric discharging problem. The PIC simulation of W-band gyro-TWT interaction structure has been carried out to see the multimode behavior of wave particle interaction. The electrostatic analysis of single stage depressed collector with nonlinear taper stage has been done to further enhance the efficiency of the gyro-TWT. The EGUN beam optics code is used for the electrostatic simulation of electron beam in the collector region. Further, the design goal for the present W-band gyro-TWT along with various subassemblies is listed out in Table 4.1.

The one of the objectives of the present work is to improve the overall efficiency of W-band gyro-TWT. The electronic efficiency of gyro-TWT highly relies upon the quality of the electron beam from the magnetron injection gun (MIG). The electron beam having low axial velocity spread and optimum velocity ratio is required to achieve the high electronic efficiency in gyro-TWTs. A triode type MIG allows more parameter space to adjust the velocity spread due to additional control anode. Further, an energy recovery system for recovering the spent electron beam energy can improve the overall efficiency. The depressed collector is widely used as an energy recovery system in conventional TWTs and gyrotron [Yang *et al*. (2019), [Zhang *et al.* (2009)]. It converts the kinetic energy of the spent beam into electric and heat energy. The electrical energy is recovered through the loop current, while heat energy is dissipated on the collector wall. The present work is organized as follows: Section 4.2 discusses the design of triode type MIG. Section 4.3 presents the design and analysis of periodically loaded RF interaction circuit for W-band gyro-TWT. In Section 4.4, the 3D PIC simulation results and their validation of the present gyro-TWT are elaborated. A 3-stage depressed

collector as an energy recovery system and double disk RF output window for the present W-band gyro-TWT are presented in section 4.5 and the summary of the present work is drawn in section 4.6.

Table 4.1: Design goal of the various component of Gyro-TWT

Component	Design Goal of fundamental TE_{01} mode W-band gyro-TWT
Output	P_0 =~200kW, efficiency = ~30 %
MIG	V_0 = 70kV, I_0 = 10A, velocity spread < 3%, velocity ratio = ~ 1.2
Input Coupler	Wrap around type coaxial TE_{01} mode input coupler with minimum reflection and high transmission over the operational bandwidth
RF interaction Circuit	Periodic dielectric loaded to avoid the discharging problem
Collector	3-stage depressed collector to improve the overall efficiency
Output window	Triple disk window of operational bandwidth between 90-100GHz

4.2. Design of Triode Type Magnetron Injection Gun

In the present study of W-band gyro-TWT a double anode (triode) MIG is used to facilitate the gyro-TWT with minimum axial velocity spread and to provide the extra control to adjust the beam parameters. The electronic efficiency of gyro-TWT can be improved by using the electron beam having minimum axial velocity spread, velocity ratio slightly greater than unity and selecting the beam guiding center near the maximum electric field strength for strong beam-wave interaction. To meet these requirements imposed by beam-wave interaction circuit, a triode type MIG is selected for W-Band gyro-TWT operating at 70 kV, 10 A. The initial design parameters of the electron gun, including the emitter radius (r_c), cathode slant angle (θ_c) and magnetic compression ratio (F_m), are calculated using the trade-off equations [Baird and Lawson (1986)]. These equations are based on the conservation of angular momentum and

adiabatic assumptions. The design parameters of MIG based on the trade-off equation are listed in Table 4.2. Figure 4.1 shows the trade-off between F_m and B_c for different values of r_c using one of the tradeoff equations given by,

$$F_m = B_0 / B_c = r_c^2 / (r_g^2 - r_L^2) \tag{4.1}$$

where, F_m is the ratio of the magnetic fields in the RF interaction region (B_0) and at the cathode (B_c), while r_g and r_L are the guiding center and Larmor radii of the electron beam, respectively. The large is the value of r_c, the higher is the required compression ratio and vice-versa. To avoid the interception of the beam with the drift tube, the maximum beam radius must satisfy,

$$r_{b\max} \cong F_m^{0.5} r_{cu} + r_L \tag{4.2}$$

where, r_{cu} is the upper emitter radius and γ is the relativistic mass factor. The Larmor radius (r_L) is given as,

$$r_L(\text{mm}) = 17.03\,(\alpha^2(\gamma^2 - 1) / ((1+\alpha^2) B_0(kG)) \tag{4.3}$$

The lower radius of the emitter strip can be evaluated from $r_{cl} = \sqrt{(r_{cu}^2 - I_0 \sin\theta_c / J_c\, \pi)}$, where, J_c is the cathode current density, I_0 is the beam current and α is the axial to transverse velocity ratio. The double anode configuration is employed rather than single anode geometry. The modulating anode voltage facilitates the adjustment of the velocity spread and velocity ratio irrespective of the magnetic field [Nguyen *et al.* (2001)]. The optimum value of axial velocity spread and velocity ratio is obtained by optimizing the MIG geometry and design parameters using the tracking solver of "CST-Particle Studio". The simulated results (Table 4.2) of the present MIG demonstrate a good quality of electron beam with less than 2% axial velocity spread and velocity ratio of 1.12. The velocity spread due to roughness of cathode surface and cathode temperature is neglected, *i.e.* assuming an ideal cathode.

Table 4.2 Triode MIG optimized parameters and simulated results

Triode MIG Design parameters	
Emitter radius	5.05 mm
Guiding center radius	0.965 mm
Maximum beam radius	1.25 mm
Emitter angle	48^{o}
Mod-anode voltage	17.5 kV
Cathode loading	8.38 A /cm^2
Compression ratio	27
Circuit magnetic field	3.45 T
Triode MIG simulated results	
Average velocity ratio	1.12
Axial velocity spread	2.0 %
Transverse velocity spread	2.3 %
Peak anode Electric field	42 kV /cm
Peak cathode field	53 V /cm

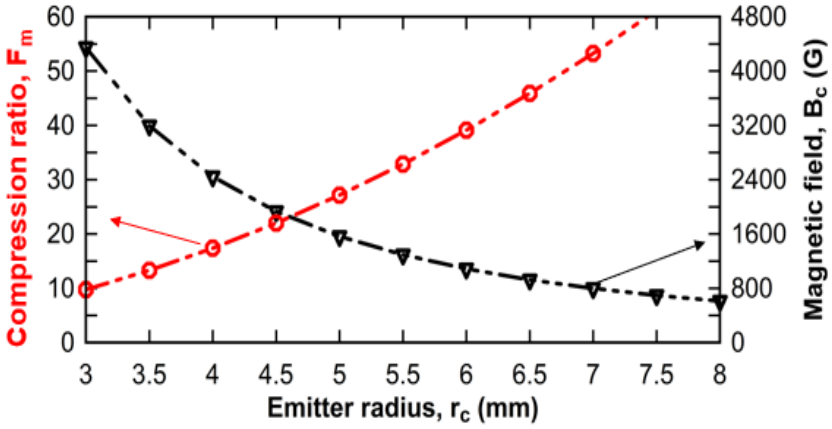

Figure 4.1 Compression ratio (F_m) and magnetic field at the cathode (B_c) Vs cathode radius (r_c).

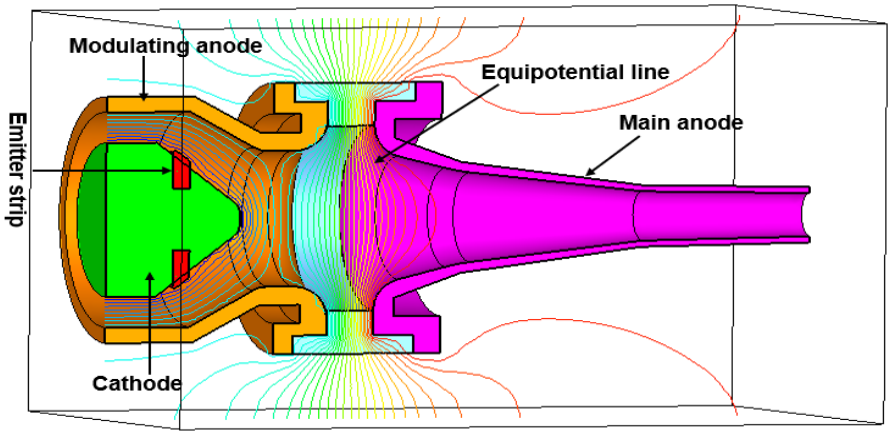

Figure 4.2 The CST model of the geometry of triode type MIG with equipotential lines.

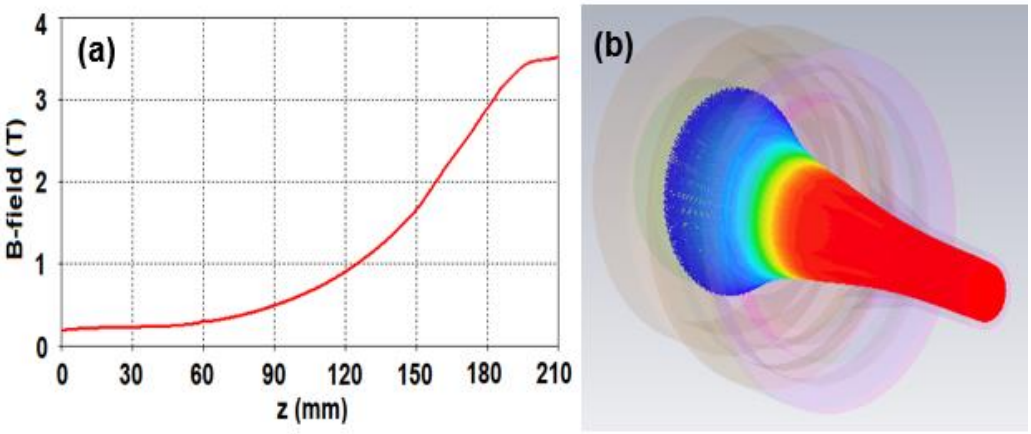

Figure 4.3 (a) Magnetic field profile of triode MIG for W-band gyro-TWT operating at 70 kV, 10 A and, (b) trajectory of the emitted beam along the axial length of MIG.

The 3D model of the triode type MIG using CST along with equipotential lines is shown in Figure 4.2. The magnetic field profile and the electron beam trajectory along the axial length of triode type MIG are shown in Figure 4.3(a) and 4.3(b), respectively.

4.3. Design of Beam Wave Interaction Structure

There are the two kinds of theoretical models for the lossy interaction waveguide system for the gyro-TWT operation, one is lossy copper interaction circuit [Chu *et al.* (1999)] and the other one is the lossy dielectric (ceramic) interaction circuit [Calame *et al.* (2002)]. Undoubtedly, the lossy copper model is simpler but still accurate enough to understand the major problems in the system. Especially, the lossy copper model has been extensively and successfully studied and reported by K. R. Chu at NTHU. About the lossy ceramic model, that is more accurate and better approximation to the real high-average power device. One should keep in mind that the ceramic-loaded circuit is with waveguide transverse area larger than that of the copper cylindrical waveguide at the same operating frequency, which means there are more challenging modes exist there and should be carefully considered in a ceramic loaded circuit. Further, the loading of the interaction waveguide can be done by two ways, one is the

uniform loading and other is the periodic loading. The uniform dielectric loaded waveguide may have the problem of dielectric charging due to the long lossy dielectric section, therefore, periodic loading is preferred in which the metal rings are generally used to avoid the potential problem of dielectric charging at the inner surface of the dielectric. In the following sub-sections, the mode mapping and dispersion in periodic dielectric waveguide for gyro-TWT, beam wave coupling impedance analysis of the operating as well parasitic backward wave oscillations and stability against the potential backward wave oscillations are presented.

4.3.1. Mode Mapping and Dispersion of PDL waveguide

The dispersion relation of a lossy dielectric waveguide can be obtained by using the following transcendental equation:

$$\left[\frac{1}{k_{\perp \mathrm{I}}}\frac{J_m'(k_{\perp \mathrm{I}}r_\omega)}{J_m(k_{\perp \mathrm{I}}r_\omega)}-\frac{1}{k_{\perp \mathrm{II}}}\frac{\mu_{II}}{\mu_I}\frac{P'(k_{\perp \mathrm{II}}r_\omega)}{P(k_{\perp \mathrm{II}}r_\omega)}\right].\left[\frac{1}{k_{\perp \mathrm{I}}}\frac{J_m'(k_{\perp \mathrm{I}}r_\omega)}{J_m(k_{\perp \mathrm{I}}r_\omega)}-\frac{1}{k_{\perp \mathrm{II}}}\frac{\varepsilon_{II}}{\varepsilon_I}\frac{Q'(k_{\perp \mathrm{II}}r_\omega)}{Q(k_{\perp \mathrm{II}}r_\omega)}\right] - \frac{1}{\mu_1\varepsilon_1}\left(\frac{k_z m}{\omega r_\omega}\right)^2\left[\frac{1}{k_{\perp \mathrm{I}}^2}-\frac{1}{k_{\perp \mathrm{II}}^2}\right]^2 = 0 \tag{4.4}$$

For a mode with $k_z = 0$ and azimuthal index, m = 0, equation (4.4) is decoupled for *TE* and *TM* modes.

$$\left[\frac{1}{k_{\perp \mathrm{I}}}\frac{J_m'(k_{\perp \mathrm{I}}r_\omega)}{J_m(k_{\perp \mathrm{I}}r_\omega)}-\frac{1}{k_{\perp \mathrm{II}}}\frac{\mu_{II}}{\mu_I}\frac{P'(k_{\perp \mathrm{II}}r_\omega)}{P(k_{\perp \mathrm{II}}r_\omega)}\right] = 0 \qquad \text{for } TE \text{ mode} \tag{4.5}$$

and,

$$\left[\frac{1}{k_{\perp \mathrm{I}}}\frac{J_m'(k_{\perp \mathrm{I}}r_\omega)}{J_m(k_{\perp \mathrm{I}}r_\omega)}-\frac{1}{k_{\perp \mathrm{II}}}\frac{\varepsilon_{II}}{\varepsilon_I}\frac{Q'(k_{\perp \mathrm{II}}r_\omega)}{Q(k_{\perp \mathrm{II}}r_\omega)}\right] = 0 \qquad \text{for } TM \text{ mode} \tag{4.6}$$

For $k_z \neq 0$ and $m \neq 0$, the solution of equation (4.4) results in hybrid $HE_{m,n}$ or $EH_{m,n}$ modes. As each period of periodic dielectric-loaded waveguide contain two sections, namely, a dielectric section and a copper region. The modes will have complex field

distribution. The transverse field distribution of TE_{11}, TE_{21}, TE_{01}, and TE_{02} mode in the dielectric section, maps to the modes that in the uniform DL waveguide *i.e.*, HE_{12}^{d}, HE_{22}^{d}, TE_{02}^{d}, and TE_{04}^{d} [Figure 4.4], while in the copper region, modes are similar to that in the conventional copper waveguide [Table 4.3]. Due to such a mapping relationship, four modes namely, ~TE_{11}, ~TE_{21}, ~TE_{01}, and ~TE_{02}, are used for the mode's nomenclature in the periodic dielectric waveguide [Du *et al.* (2009), (2014)].

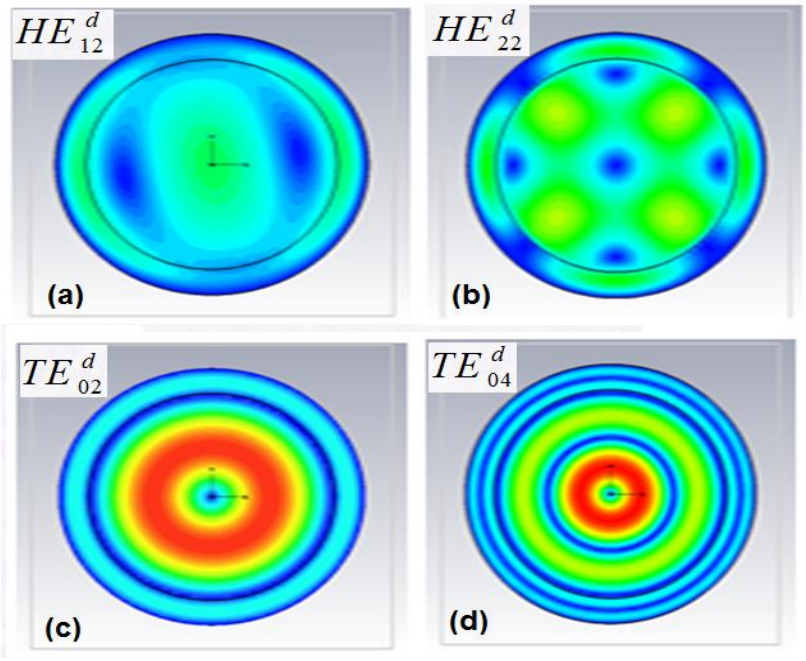

Figure 4.4 Contour plots of various mode in lossy dielectric loaded waveguide.

The solution of the dispersion equation (4.4) for real ω is having a complex wave number (k_r+jk_i) with $|k_i| >> k_r$ near the cut-off region. Therefore, the dispersion curve of modes is discontinuous near the cut-off region due to high attenuation by the lossy dielectric [Figure 4.5(a)]. The grazing intersection of waveguide ~TE_{01} mode with fundamental beam mode line (s =1) in the forward direction ($k_z > 0$) represents the operating point of the present gyro-TWT that causes convective instability near the cut-off, hence the amplification of wave occurs. However, an intersection in the backward-wave region ($k_z < 0$) causes absolute instabilities and BWOs, which has an adverse

effect on the performance of gyro-TWT. The attenuation characteristics of both operating and competing modes [Figure 4.5(b)] in lossy waveguide shows that the lossy material provides an attenuation ~20.5 dB /cm to the operating TE_{01} mode, 18.5 dB /cm to TE_{11} mode, ~30 dB /cm to TE_{21} mode, and 33.60 dB /cm to TE_{02} mode at their respective frequency of oscillation. It is observed that TE_{11} mode posses minimum attenuation, as it intersects with the beam mode line at higher k_z value and attenuation of TE_{02} mode is higher, as it intersects near to the cut-off, *i.e*. lower k_z region.

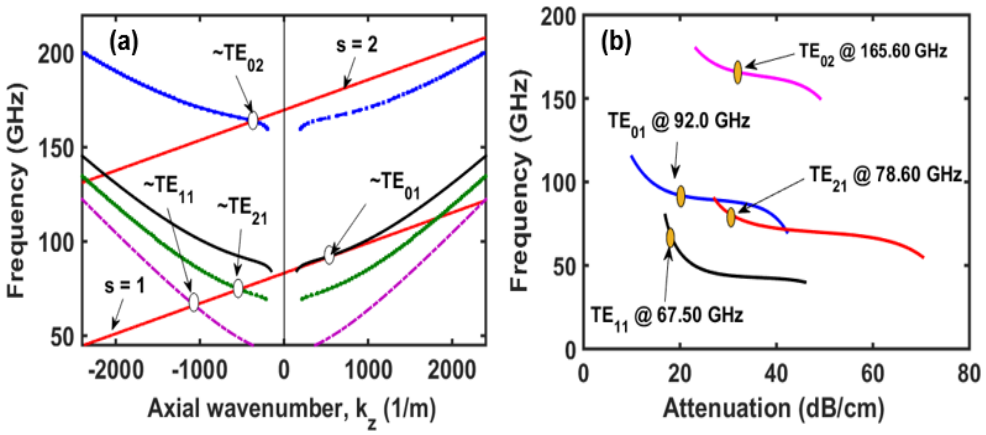

Figure 4.5 (a) Dispersion diagram of operating TE_{01} (for both lossy and lossless waveguide) along with the nearby competing modes, and (b) attenuation of operating and competing modes by the lossy dielectric.

Table 4.3 The mode mapping between smooth cylindrical waveguide, uniform DL waveguide and periodic DL waveguide.

Smooth waveguide	TE_{11}	TE_{21}	TE_{01}	TE_{02}
Uniform DL waveguide	HE_{12}^{d}	HE_{22}^{d}	TE_{02}^{d}	TE_{04}^{d}
Periodic DL waveguide	~TE_{11}	~TE_{21}	~TE_{01}	~TE_{02}

4.3.2. Beam-wave Coupling Impedance

The coupling impedance [Du *et al.* (2010)] of gyro-TWT is computed to study the strength of coupling between the electron beam and various waveguide modes including the operating and BWO modes. The coupling impedance can be defined as,

$$K_0 = \mu_0 \frac{H_{sm}}{G_1 + G_2} \frac{r_L^2}{s^2} \upsilon_p \tag{4.7}$$

where, $H_{sm} = | J_m^{'}(k_{t1} r_L) J_{m-s}(k_{t1} r_g) |^2$ is the beam wave coupling factor, μ_0 is the permeability of the vacuum, r_L is the Larmor radius of the electron beam, v_p is the phase velocity of the operating mode, s is the harmonic number, and G_1 and G_2 are power factors corresponding to vacuum and dielectric regions in an RF interaction circuit, respectively. Since the coupling impedance (K_0) is directly proportional to the phase velocity of the wave, its value is maximum near the cut-off region ($k_z \sim 0$) and K_0 is also proportional to H_{sm}, which is consistent with the radial position of the electron beam. The coupling impedances of operating TE_{01} mode and its competing modes are plotted as a function of normalized guiding center (r_g / r_w) [Figure 4.6(a)]. In the present design, the guiding center radius is chosen as $r_g = 0.48\ r_w$ at which the coupling impedance is maximum for the desired operating TE_{01} mode. Figure 4.6(b) depicts the coupling impedance and growth rate of the operating TE_{01} mode in both loaded (lossy) and unloaded (lossless) sections of the RF interaction circuit as a function of frequency. It is observed that both growth rate and coupling impedance are reduced in the lossy section due to heavy attenuation.

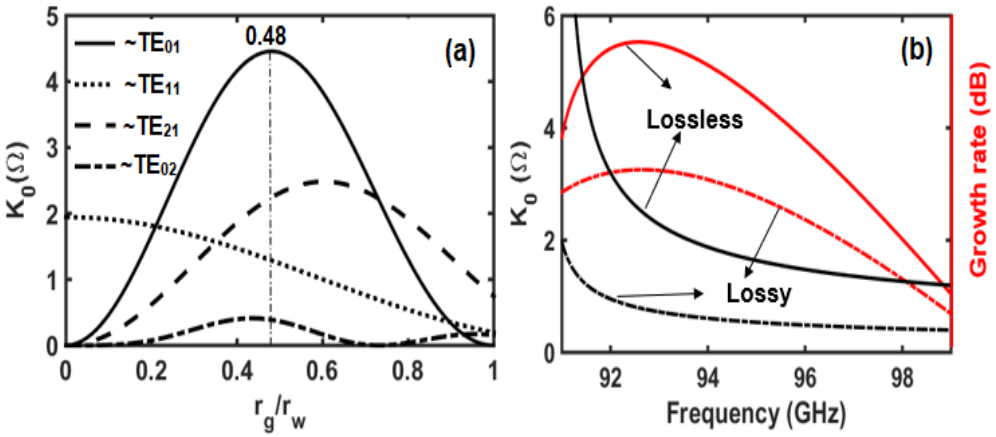

Figure 4.6 (a) Coupling impedance (K_0) of operating and spurious modes as a function of normalized guiding center radius, and (b) K_0 and growth rate of operating mode in lossy and lossless waveguide.

4.3.3. BWOs Study and Stability Analysis

The periodic dielectric loading technique is employed in the present RF interaction circuit (Figure 4.7) of the gyro-TWT amplifier. In periodic structures, fields in adjacent periods are given by using Floquet's theorem as described by Tigelis *et al*. [Tigelis *et al.* (1998)]. The cross-section of PDL waveguide is divided into two regions namely: (i) vacuum region (R_1), and (ii) dielectric region (R_2). In region R_1, the wave is propagating one; therefore, the axial magnetic field in R_1 is expressed as a sum of Bloch harmonics. In region R_2, the axial component of the magnetic field corresponds to standing Eigen waves, which are expressed by using Fourier series. In order to characterize the transverse field equation for the present periodic dielectric waveguide, the relevant boundary conditions are incorporated. The tangential electric and magnetic fields must be continuous at the interface between region (R_1) and region (R_2), *i.e.* at $r = r_{w,}$ as given by

$$E_{\varphi}^{I} = E_{\varphi}^{II} \quad \text{and} \quad H_{z}^{I} = H_{z}^{II} \qquad \text{for } 0 \le z < b \tag{4.8}$$

The tangential electric field should vanish at the interface between vacuum and perfect conductor, at $r = r_w$ as given by

$$E_{\varphi}^{I} = 0 \qquad \text{for} \quad b + nL \le z < (n+1)\,L \tag{4.9}$$

The tangential electric field should also vanish for the interface between dielectric and perfect conductor at $r = r_w + d$,

$$E_{\varphi}^{II} = 0 \qquad \text{for } 0 \le z < b \tag{4.10}$$

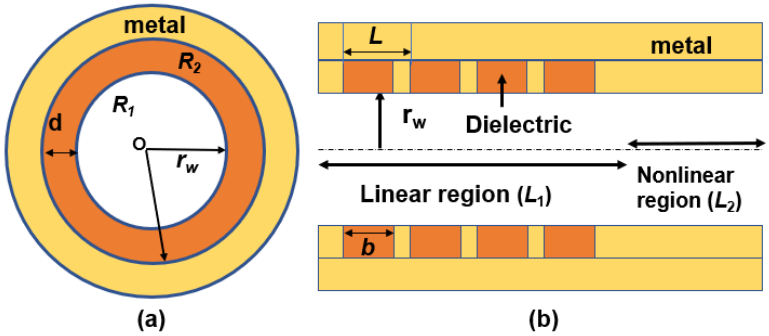

Figure 4.7 (a) Transverse and (b) axial schematic view of a periodically loaded RF interaction structure for W-band gyro-TWT.

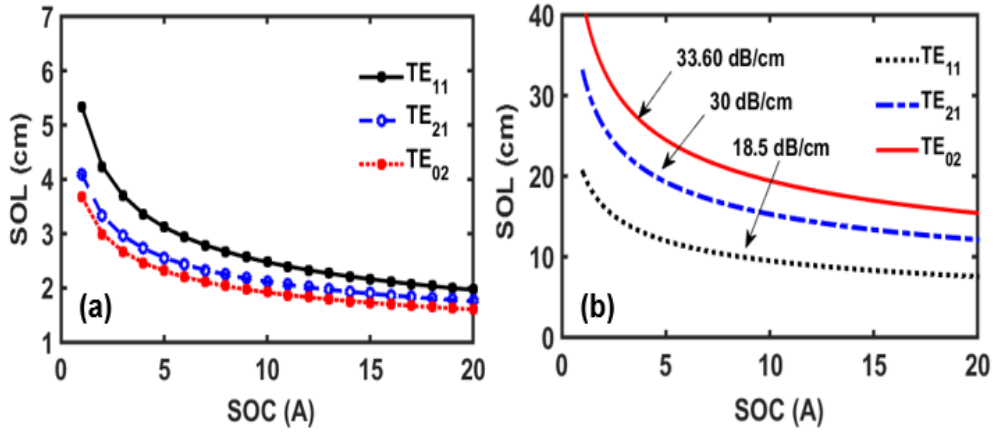

Figure 4.8 SOL Vs SOC of competing modes in (a) loss-free unloaded section, and (b) lossy dielectric-loaded linear section.

The present circuit consists of three sections namely: a short copper waveguide section at the upstream that is followed by a long lossy linear section and a copper waveguide (nonlinear section) at the downstream of the RF interaction circuit. To suppress the spurious BWO modes, the length of the copper sections needs to be chosen carefully. Linear theory [Kou *et al.* (1992)] is used to obtain the relation between the start oscillation length (SOL) of oscillating modes and their SOC in the unloaded copper section. Figure 4.8(a) shows the SOL of spurious TE_{11}, TE_{21}, and TE_{02} modes with respect to their start oscillation current. It is observed that SOL of spurious modes decreases as the beam current increases and vice versa. Among all considered spurious modes, as TE_{02} mode is having least SOL ~2 cm for a fixed beam current ~10A, that is highly susceptible to oscillation. Therefore, for the stable operation, the copper section

length must be less than the SOL of TE_{02} mode. In order to achieve the desired power and gain, the length of the RF interaction circuit should be long enough. Therefore, a lossy linear section is added to a lossless nonlinear section of the RF interaction circuit. The length of the lossy linear section is calculated using the transmission loss characteristics of spurious modes [Figure 4.8(b)]. SOL of TE_{11}, TE_{21}, and TE_{02} modes are calculated as ~10 cm, ~16 cm, and ~20 cm for the attenuation loss ~18.5 dB /cm, ~30 dB /cm, and 33.60 dB /cm, respectively [Figure 4.7(b)]. The length of the lossy linear section is chosen below the SOL of backward competing modes. Using dielectric loading, SOC of spurious modes is increased to a value higher than the operating current of ~10 A. Thus, the excitation of these spurious backward wave oscillations is restricted.

4.4. PIC Simulation and Validation

To evaluate the performance of the present gyro-TWT, the RF interaction circuit is modeled and simulated in a commercially available 3D electromagnetic code "CST-Particle Studio". The design parameters of gyro-TWT are listed in Table 4.4. Firstly, a cylindrical copper waveguide with radius (r_w) is modeled. For the lossy linear section, periodic grooves of 9 mm length and thickness (d) are cut on the inner surface of the copper waveguide. The dielectric rings of BeO-SiC material are then inserted into these grooves. The separation between each groove is kept 2.0 mm to avoid the dielectric charging. The length of the unloaded input and output copper section is 8 mm and 18 mm, respectively. The TE_{01} mode input signal is excited at the input port. During the PIC simulation, the gyrating electron beam started to interact with various waveguide modes, but as the lossy linear section provides the heavy attenuation to the waveguide modes, the spurious modes get easily suppressed. The electric field strength of the amplified operating mode (TE_{01}) is shown in Figure 4.9(a). The Fourier transform of the

amplified output signal shows a peak at 92 GHz without any mode competition [Figure 4.9(b)]. After the post-processing in CST, the simulation predicted an instantaneous power of ~406 kW or simply ~203 kW of actual output power (averaged over an RF period) in the operating TE_{01} mode at 92 GHz [Figure 4.10(a)]. The simulation results are validated using nonlinear multimode theory [Tang *et al.* (2017)]. The steady-state growth of power in operating and spurious modes is obtained using multimode code [Figure 4.10(b)]. Due to the heavy attenuation in the lossy linear section, the power growth is less and it mainly grows exponentially in the nonlinear section. The multimode code predicted ~200 kW of power in the operating TE_{01} mode and negligible power (few watts) in spurious modes, due to heavy attenuation provided by lossy linear section. The calculated power in the operating TE_{01} mode using PIC simulation and multimode codes are agreed by ~4 %. Further, parametric studies on the output power with respect to frequency for different velocity spread and different length of RF interaction has been carried out. For an ideal electron beam (0 % axial velocity spread), a bandwidth of ~5.4 GHz is achieved with more than 100 kW output power. Both bandwidth and output power of the amplifier is reduced as the axial velocity spread is increased. The bandwidth is reduced to ~4.8 GHz and ~3.8 GHz and output power is reduced to 185 kW and 159 kW for 2 % and 4 % spread in axial velocity, respectively [Figure. 4.11(a)]. The length of the nonlinear section of the RF circuit is varied by fixing the input copper section and linear section lengths. The power output for different RF circuit length is observed [Figure. 4.11(b)] that shows the maximum power and bandwidth at a length of 112 mm *i.e.,* (18 mm length of the nonlinear section). The maximum amplification of the RF wave does not occur below 112 mm length; therefore gyro-TWT delivered less output power. Above 112 mm length, the power is transferred to spurious modes, therefore output power in the operating mode starts decreasing.

Table 4.4 Design parameters of W-band PDL Gyro-TWT

Parameters	**Value**
Beam Voltage, V_0	70 kV
Beam Current, I_0	10.0 A
Velocity Pitch Factor	1.12
Waveguide radius, r_w	2.02 mm
Lossy dielectric thickness	0.55 mm
Guiding center radius, r_g	0.48* r_w
Operating Mode	TE_{01}
Dielectric material (BeO-SiC)	10.0 – j3.9
DC Magnetic Field, B_0	3.435T
Input copper section	8 mm
Lossy section	86 mm
Output copper section	18 mm

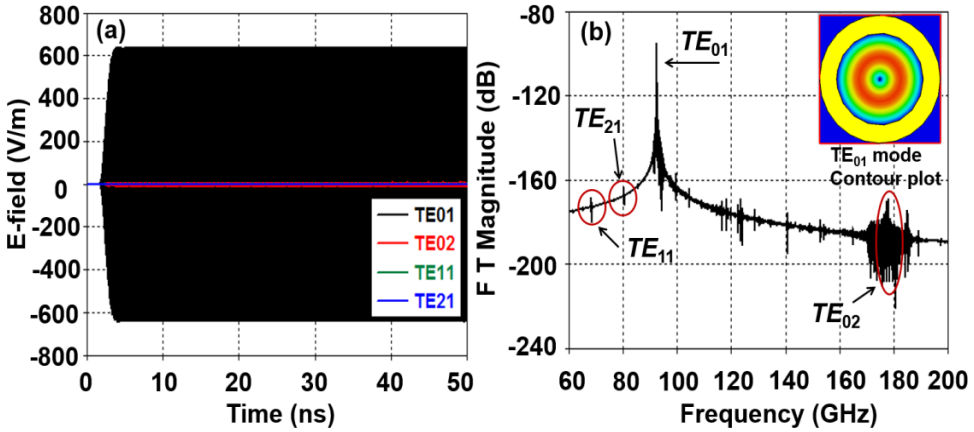

Figure 4.9 (a) Temporal growth of TE_{11}, TE_{21}, TE_{01} and TE_{02} modes at the output port, (b) Frequency spectrum of the output signal.

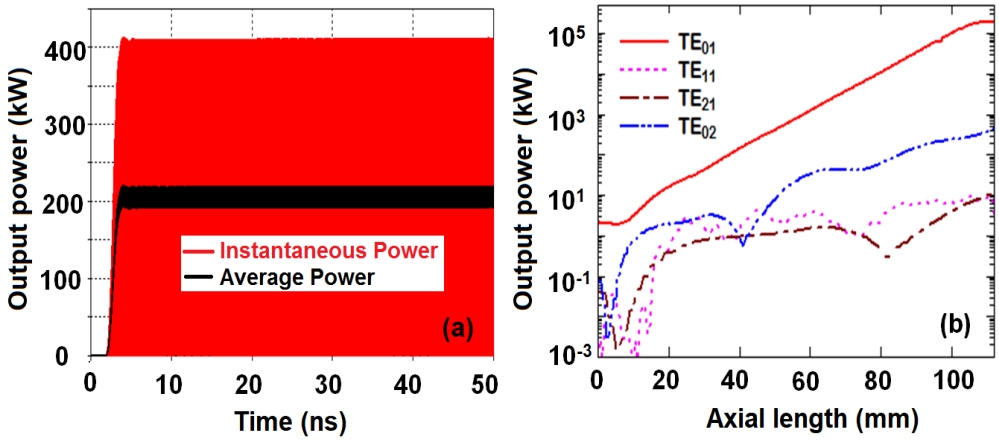

Figure 4.10 (a) Temporal growth of instantaneous output power (red) and averaged power (black) in TE_{01} mode using CST and (b) spatial growth of output power in various modes using multimode theory.

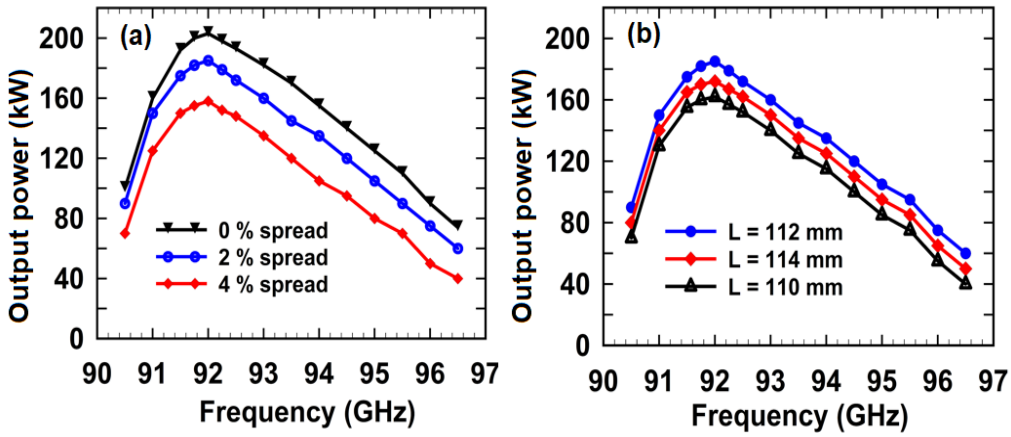

Figure 4.11: Output power Vs frequency (a) for 0%, 2%, and 4% axial velocity spread and (b) for different values RF circuit length at 2 % axial velocity spread.

4.5. Design of Output System

4.5.1. Depressed collector for Gyrotron Devices

The major enhancement in the efficiency of gyrotron devices is possible through the depressed collectors. In all gyrotron devices only the transverse rotational energy of gyrating electron beam is converted into RF energy [Ghosh *et al.* (2007)]. This fundamentally imposes the limitation on the overall efficiency of gyrotron devices, because the axial energy of electron beam is not participating in the interaction process. In a depressed type collector, a potential depression with respect to the main body potential is applied in the collector region to regain the axial kinetic energy of the spent

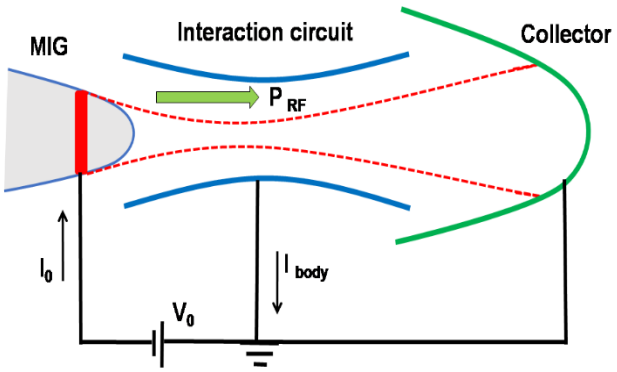

Figure 4.12: Schematic of gyro device with undepressed collector.

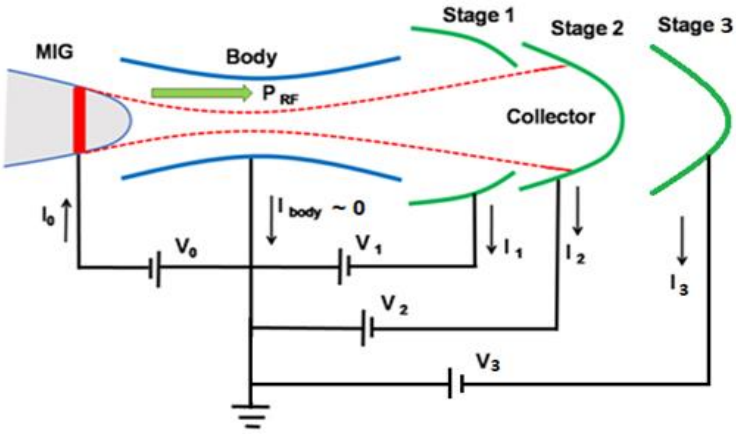

Figure 4.13: Schematic of gyro device with 3-stage depressed collector.

electron beam. The energy of the unused electron beam is decelerated by this potential depression and extracted in the form of current through the depressed electrode. In this way, not only overall efficiency greatly improved but also the power loading on the collector surface is greatly reduced [Ghosh *et al.* (2007), Zhang *et al.* (2009), (2011)]. In this way, the long-pulse operation of gyrotron devices greatly facilitated and the possibility of collector failure due to metal fatigue is greatly reduced. In an undepressed type collector, the collector potential is same as the potential of main body and electrons dissipate their total kinetic energy on the collector as heat only. The concept of depressed collector can be understood with the help of its electrical circuit. Figure 4.12 depicts a conventional microwave tube with undepressed type collector, in which the DC power $P = V_0 I_0$ is supplied to the cathode and a microwave power of P_{RF} is generated. Assuming that the whole circuit is in no loss and there is no other power supply except the power supply between the MIG and main body. Then, the efficiency of the conventional gyrotron device without the depressed collector can be written as,

$$\eta_{\text{int}} = P_{RF} / P_{DC} \tag{4.11}$$

where, P_{RF} is generated microwave power after the beam wave interaction process at the end of interaction structure and P_{DC} is the DC power contained by the electron beam. The difference of P_{DC} and P_{RF} is contained by the spent beam which will finally be

dissipated on the collector wall as heat. Figure 4.13 shows a configuration of tube with 3-stage depressed collector. The main power supply of V_0I_0 is connected between the cathode and body and other power supplies are connected to the cathode through depressed electrodes for creating the potential depression. As most of the electrons pass through the microwave structure, the body current will be very less ($I_{body} \sim 0$). The total electron beam power collected at the electrodes of depressed collector can be calculated as [Zhang *et al.* (2009)],

$$P_{col} = V_1 I_1 + V_2 I_2 + V_3 I_3 \tag{4.12}$$

where, V_1, I_1 and V_2, I_2 denote the potential and collected beam current at the electrode of stage1 and stage2, respectively. The electronic efficiency η_e is defined as,

$$\eta_e = P_{RF} / P_{DC} \tag{4.13}$$

After the RF interaction the remaining beam power of spent electrons is given by,

$$P_{spent} = P_{DC} - P_{RF} \tag{4.14}$$

This spent beam energy needs to be collected by introducing number of stages in the depressed collector. Thus, the collector efficiency can be defined as,

$$\eta_{col} = \frac{P_{col}}{P_{spent}} \tag{4.15}$$

The efficiency of depressed collector can be increased by increasing the number of stages; however, it will increase the complexity of the design. The overall efficiency, $\eta_{overall}$ of gyro-TWT after introducing the depressed collector and can be defined as [Zhang *et al.* (2011)],

$$\eta_{overall} = \frac{P_o}{P_{DC} - P_{col}} = \frac{\eta_{out}\,\eta_e}{1 - \eta_{col}\,(1 - \eta_e)} \tag{4.16}$$

where, P_o is the RF output power after considering RF losses, for example ohmic wall losses, η_{out} is the output efficiency and calculated as $\eta_{out} = P_o / P_{RF}$. Based on the relation shown in (4.16), Figure 4.14 shows the overall efficiency of gyrotron devices as a function of electronic and collector efficiencies. This shows that irrespective of the electronic efficiency of gyro-TWT, 10 % increase in η_{col} leads to an improvement of nearly 5 % in $\eta_{overall}$.

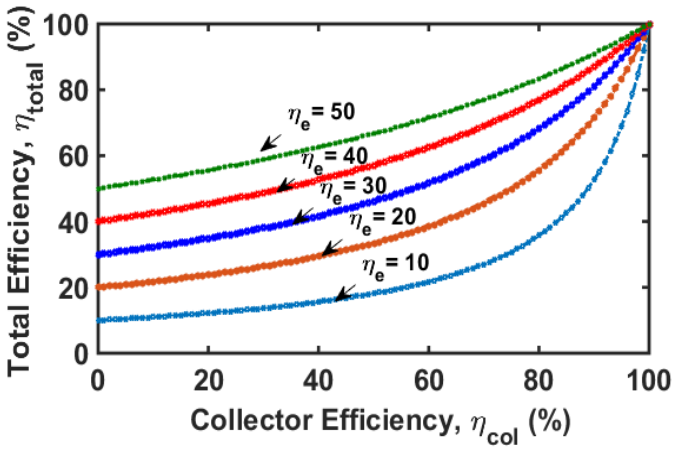

Figure 4.14: Relation between the total efficiency and electronic efficiency of gyro-TWT as a function of collector efficiency

4.5.2. Design of 3-Stage Depressed Collector using 'MAGIC 3D'

A three-stage depressed collector has been designed and simulated to recover the spent beam energy for the present ~200 kW W-band TE_{01} mode gyro-TWT amplifier using PIC simulation code 'MAGIC'. Before simulate the depressed collector, an electrodynamics model was simulated using 'MAGIC 3D' for studying the beam wave interaction with the same design and electrical parameters as listed in Table 4.4. The present model of beam-wave interaction consists of RF interaction circuit, a nonlinear taper section and an output waveguide section (serving as beam collector) as shown in Figure 4.14. The linear section of the RF interaction circuit has been loaded periodically with lossy dielectric rings to suppress the potential BWOs. The output power is

measured at the end of nonlinear taper section. The PIC simulation results of the PDL TE_{01} mode gyro-TWT using 'MAGIC' predicted an output power of ~200 kW at the operating frequency which agreed well with both multimode and CST simulation results. Figure 4.15(a) shows the phase-space plot of the electron beam in the RF interaction region. It clearly depicts that in the linear section the energy of electrons is almost constant and equal to 70 keV. However, in the nonlinear section majority of electrons lose their energy (< 70 keV) to the RF wave, while few electrons gain energy (> 70 keV) from the RF wave. Figure 4.15(b) also illustrates that in the linear section the DC electron beam power (V_0I_0) is constant and equal to 700 kW, in the nonlinear section electrons lost nearly 200 kW kinetic energy to the RF wave. The remaining energy of the spent electron beam is then dissipated as heat on the inner wall of the output waveguide section serving as the undepressed (conventional) collector. After the beam wave interaction process, the spent electron beam at the end of nonlinear taper section has been exported from "MAGIC" 3D PIC simulation of PDL interaction circuit using "EXPORTBEAM" command [Figure 4.14]. Now, this spent electron beam data has been used as the input for the simulation of three stage depressed collector. The 2D model of the depressed collector and spent electron beam trajectory in the depressed collector are shown in Figure 4.16. After the simulation of collector, the electron beam current collected by depressed electrode is saved in the output data file. The spent electron beam power recovered by each electrode is calculated by multiplying the electrode potential and average beam current collected by the electrode. The collection efficiency of each stage with respect to the electrode potential is shown in Table 4.5. The overall efficiency of the present gyro-TWT in combination with 74 % collection efficiency of 3-stage depressed collector is improved from ~29 % to ~61 %.

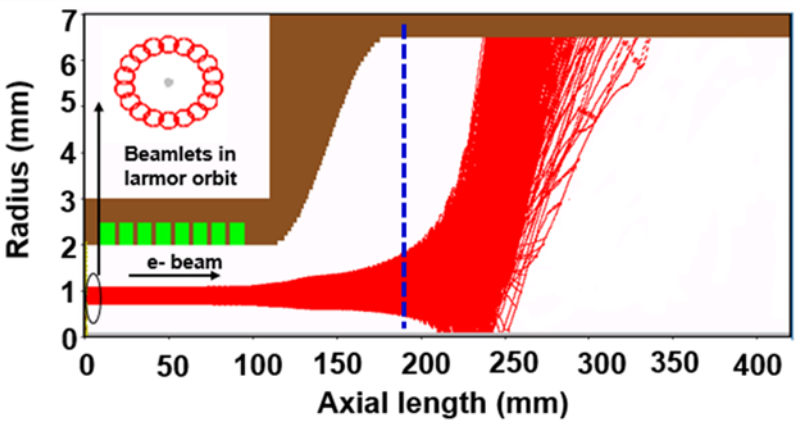

Figure 4.15: Electron beam trajectory along the axial length of the interaction structure.

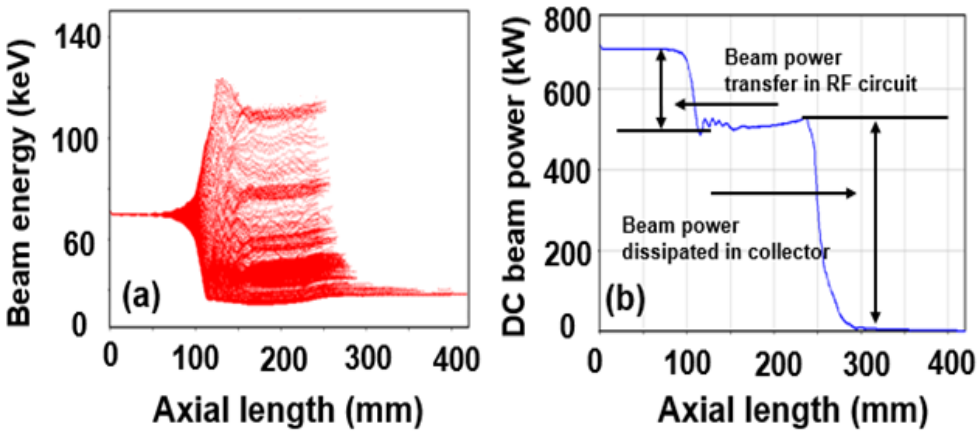

Figure 4.16: (a) Energy phase space plot of particles, and (b) DC beam power along the axial length of RF interaction structure.

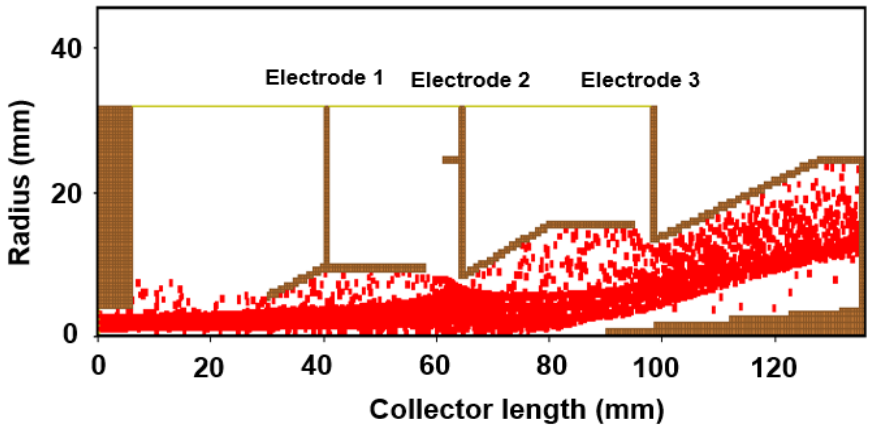

Figure 4.17: Trajectory of the spent electron beam in the collector region.

Further, the heat wall loading on the conducting electrode is calculated by using "OBSERVE COLLECTED POWER". The heat dissipated on the electrode surface is divided by the beam striking area of the conducting electrode to get the surface heat

power density. The heat wall loading of the present depressed collector is calculated as ~0.47 kW /cm^2.

$$\eta_{Total} = \frac{\eta_e}{1-\eta_{col}\,(1-\eta_e)} = \frac{0.29}{1-0.74\,(1-0.29)} = \sim 61\%$$

TABLE 4.5
COLLECTION EFFICIENCY FOR DIFFERENT ELECTRODES

Stage	Electrode potential (kV) (with reference to body potential)			Collection efficiency
1	-24	--	--	28 %
2	-24	-47	--	63 %
3	-24	-47	-70	74 %

4.5.3. Triple Disc Output window

The single or double-disc window has good transmission property but the bandwidth is narrow. Therefore, a three-disc ceramic window is designed to provide minimum reflection and good transmission over the wide frequency band. Also, the three-disc window has the advantage of high- power handling capability and wide bandwidth as compared to single- and double-disc window [Pershing et al. (2004), Lin *et al*. (2007)]. Gyro-TWT requires a wide bandwidth output window to extract the output power over the wide frequency range. The CST model of the present window is shown in Figure 4.17(a). Three ceramic discs are inserted into the circular waveguide of a 7.5 mm inner radius. The thickness (t_1) of each disc is 0.515 mm, and the separation between two adjacent discs is 0.80 mm. The cold simulation characteristics [Figure 4.17(b)] of the present RF output window shows that it has ~0.1 dB transmission loss and more than 60 dB reflection loss at 92 GHz. A good transmission bandwidth of ~15 GHz is observed. The thermal analysis is also carried out for thermal stability of the output window and observed that some amount of RF power is absorbed by the window

disc due to its finite loss tangent. The power absorbed by output window including RF reflections can be given as [Kesari *et al.* (2016)].

$$P_{abs} = (P_o\, n\, \pi\, t_1\, D \tan\delta\, (\varepsilon_r + 1)) / (100 \times c) \tag{11}$$

where, $\tan\delta$ and ε_r are the loss tangent and relative permittivity of the window disc material. *D* is the duty cycle of the gyro-TWT and *c* is the speed of light. For an RF output power load of 203 kW, the heat load of ~124 W (power absorbed) is calculated for a 10% duty cycle taken into account. The heat load is given as the input for thermal analysis. The ambient temperature of 20^0C, water flow rate 4 L /min and film coefficient of 6000 /m^2 ^{0}C has been applied. The mesh view of the window geometry modeled in ANSYS is shown in Figure 4.18(a). The maximum and minimum temperatures developed at the center and outer surface of the window are 23.78^o C and 53.79^o C, respectively [Figure 4.18 (b)].

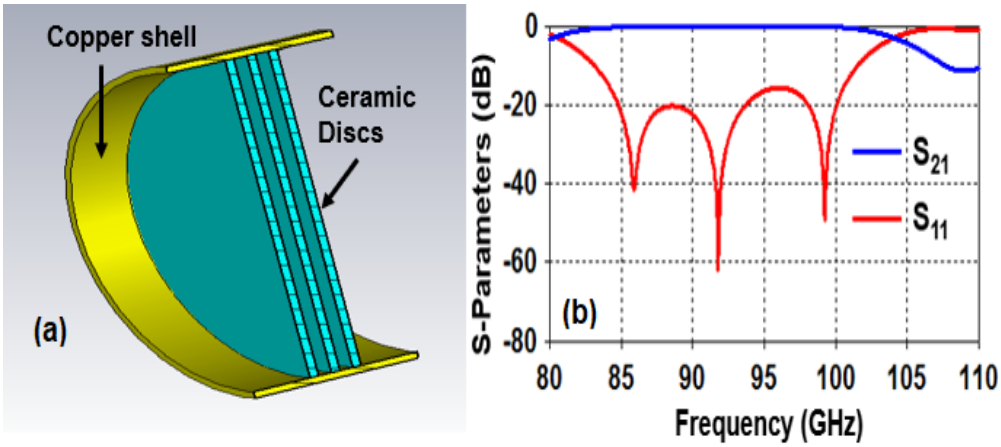

Figure 4.18: (a) CST model and (b) transmission (S_{21}) and reflection (S_{11}) coefficient for the TE_{01} mode window.

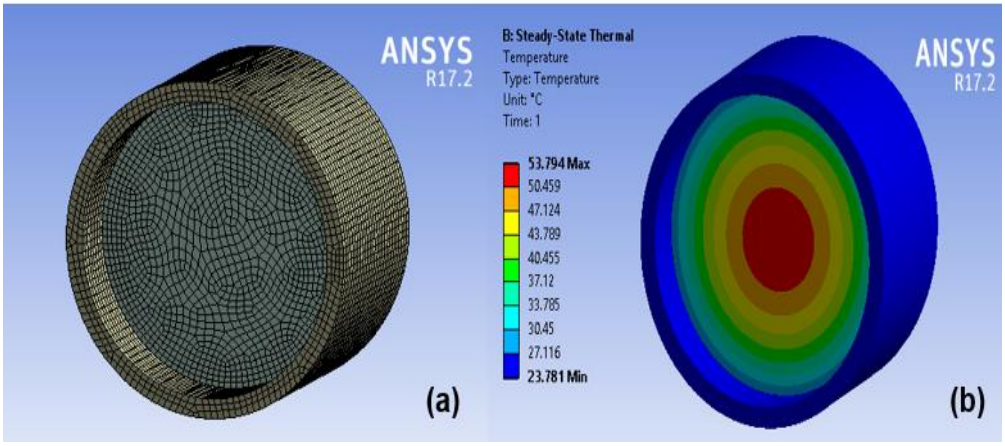

Figure 4.19: (a) Mesh view of the output window in ANSYS 17.2 and (b) temperature distribution on the window disc.

4.6. Conclusion

A millimeter-wave PDL gyro-TWT amplifier operating in TE_{01} mode at fundamental harmonic has been designed and studied. The PIC simulation predicted an RF output power of 203 kW at 92 GHz for the gyrating electron beam of 70 kV and 10A by considering 0% spread. The saturate gain, 3-dB bandwidth, and maximum power conversion efficiency have been calculated as ~57dB, ~5.4 % and ~29 %, respectively with CST simulation. The efficiency of the device is further improved by employing a 3-stage depressed collector using 'MAGIC 3D'. The spent beam is extracted from PIC simulation using 'MAGIC 3D' and given as the input to 3-stage depressed collector. The efficiency of the 3-stage depressed collector is 74% which increases the overall efficiency of the gyro-TWT from ~29% to ~61%. To extract the output power over the wide frequency range a three-disc output window has been designed and simulated. The simulation of the window has predicted a good transmission bandwidth of ~15 GHz with a reflection coefficient better than -15 dB and a minimum reflection coefficient better than -60 dB at 92 GHz. The thermal stability of both the output window and the depressed collector has been studied.